Calibration and Validation of a 3D Homogenised Damage Model for FRP Composites

Damião Tavares Costa

damiao.costa@tecnico.ulisboa.pt

Instituto Superior Técnico, Lisboa, Portugal

May 2022

Abstract

With the increasing use of fibre-reinforced polymers (FRPs) in many industries, understanding and successfully predicting the failure mechanisms of these materials is of the utmost importance. The lack of confidence in simpler criteria and the high computational costs of recent, more complete models motivated the development of a new damage progression model for pultruded FRP composites, which allows the simulation of the laminates as a homogeneous material. The present study focuses on the calibration and validation of the new model for 6 glass fibre-reinforced polymer (GFRP) materials from different suppliers. For this purpose the ABAQUS software package was used and all simulations were performed using a specific user-defined material subroutine (UMAT). The calibration was performed by adjusting the numerical curves to fit the experimental data available for different coupon tests. With all materials duly calibrated, several different application tests were simulated, and the numerical results were compared with experimental data. The calibration process was successful for all materials and coupon tests. The need to calibrate a mesh regularisation parameter with a compact tension test was also shown. For the application tests, the numerical simulations presented good agreement with the experimental data for all materials, being able to predict the failure loads, failure modes, and in some cases, even the post-failure behaviour. The results of this study show the feasibility of using the new damage progression model in structural design.

Keywords: Glass fibre-reinforced polymer (GFRP), Failure model, Damage progression, FE models, Numerical analysis.

1. Introduction

Since the second half of the 20th century, the demand for more efficient structures has led to increased research and development on composite materials, which present a better strength and stiffness-to-weight ratio than most traditional metals. With this increased use of composites, and in particular fibre-reinforced polymers (FRPs), across major industries such as aerospace, construction and automotive, there is also a need to comprehend and predict their failure mechanisms. This failure can occur on the lamina constituents - the fibres and the matrix (or even in the interface between them) - or between laminae (delamination).

To study the failure of FRPs, several theories were developed in the last century. First, non-interactive theories such as the Maximum Stress and Maximum Strain criteria were developed [1]. Then, understanding that the interaction between stresses played an important role in failure, other theories (classified as interactive failure theories) were developed, with Tsai-Hill [2] and Tsai-Wu [3] as main examples. Finally, considering these stress interactions but also developing different criteria for distinct failure mechanisms, failure mode theories such as Hashin [4] were developed. Recently, more complex theories have been developed considering also the progressive nature of laminae failure and adding the effects of delamination.

Given the lack of confidence in simpler criteria and the high computational costs of recent, more complete models, a new damage progression model for quasi-orthotropic pultruded FRP composites was developed by Gonilha *et al.* [5], which allows the simulation of the laminates as a homogeneous material. This model considers an exponential damage evolution until a limit strain is reached, followed by a constant stress stage. For an easier FE implementation, a mesh regularisation stage is added in the transition between the damage progression and the constant stress stages.

In this study, the failure model and the experimental data used is first presented. The calibration process and results are then addressed, and finally, the application tests' results used to validate the model are discussed.

2. New progressive failure model

The model's formulation is divided in two stages: (i) failure initiation, and (ii) damage propagation.

For the failure initiation, ellipsoid envelopes considering a quadratic combination of stresses are defined independently for in-plane and out-of-plane failure. Failure indexes are also defined for both in-plane (f_{pl}) and out-of-plane (f_{op}) failure. These failure indexes, which depend on the stress state imposed in the material, are used in the damage propagation stage computations.

The damage propagation stage is theoretically divided in four phases: (i) undamaged; (ii) damage progression; (iii) regularisation; and (iv) constant stress phase. The undamaged stage is characterised by linear behaviour according to the undamaged elastic modulus (E), while in the damage progression stage the elastic modulus is a function of the damage variable ($E(1-D)$) that considers an exponential damage law independent for every direction and is defined by Eq. 1:

$$D_i = d_{i,max}^{\pm} \left(1 - e^{-\frac{f_{pl}(\hat{\sigma})^{m_i^{\pm}}}{m_i^{\pm} \cdot e}} \right) \qquad (1)$$

where $d_{i,max}^{\pm}$ and $m_i^{\pm}$ are the maximum damage allowed at this stage and the exponential damage evolution control variable, respectively, for the i direction, and the failure index f_{pl} is computed for the effective stresses ($\hat{\sigma}$). For out-of-plane cases, the correspondent failure index is used (f_{op}).

However, in reality, only the damage progression stage is applied numerically until the limit strain is reached ($\epsilon_{ii,u}^{\pm}$ or $\gamma_{ij,u}$). The regularisation stage is then implemented by using a mesh regularisation parameter (α), and to avoid severe convergence difficulties in implicit analysis, viscous regularisation parameters that depend on the time step interval used are defined for every direction ($\eta_i^{\pm}$). Finally, the constant stress phase takes place, with a residual strength input defined ($r_{ii}^{\pm}$ or r_{ij}).

Summarising, the damage model requires the calibration of 64 input variables: (i) 9 elasticity inputs, including elastic and shear moduli and Poisson coefficients, (ii) 9 strength inputs, (iii) 18 damage progression control inputs ($d_{i,max}^{\pm}$ and $m_i^{\pm}$), (iv) 18 residual strength control inputs ($\epsilon_{ii,u}^{\pm}$, $\gamma_{ij,u}$, $r_{ii}^{\pm}$, and r_{ij}), 9 viscous regularization parameters ($\eta_i^{\pm}$), and (iv) 1 mesh regularization parameter (α).

3. Experimental material characterisation and application tests

The experimental data used in this work is divided in two types of tests: (i) mechanical characterisation tests; and (ii) application tests. These tests were performed for 6 different materials - I200-FC, I150-AP, I150-ST, I152-CP, U150-ST, and S120-AP. The first term refers to the type of section ("I" section, "U" section and "S" for square hollow section) and the profile height (in millimetres) from which the specimens are retrieved. The second is an abbreviation of the material's supplier.

3.1. Mechanical characterisation tests

The mechanical characterisation tests were performed to retrieve the necessary mechanical properties that are used as input in the damage progression model. Tensile tests were performed according to ISO 527, and compressive tests with a combined loading compression (CLC) test configuration, in accordance to ASTM D6441/D6641M-09, except for the S120-AP material, where the standard ASTM D695-02 was used. The in-plane shear properties were retrieved for most materials following the *Iosipescu* test standard ASTM D5379/D5379M-05. For I150-AP and S120-AP, 10° off-axis tensile tests were also performed following the recommendations in Hodgkinson [6].

Table 1 summarises the main mechanical properties for all tests and materials (for the web sections).

3.2. Application tests

Several application tests with different characteristics were performed in order to assess the validity of the damage progression model. In all tests, the required displacements were imposed and measured with an *Instron* universal test machine. Maximum load (F_{max}) and stiffness (K, measured between 10% and 20% of the maximum load) values were computed for further comparison with numerical results. These experimental results, however, are omitted for summary purposes.

For the compact tension (CT) tests, the specimens used were approximately square (60x58mm²), and two holes with 12 mm of diameter were cut near the top left and bottom left corners. The displacement was imposed to the top hole in the upwards direction, and the bottom hole was fixed with a steel pin. The specimen's notch (with 30 or 35 mm of total length) was machined with a 2 mm thick circular saw blade, except for the last 5 mm of the notch length, where a 0.6 mm thick saw blade was used. A video-extensometer measured the displacements in the crack mouth opening displacement (CMOD) points, which were placed in the same vertical axis as the centre of the holes and near the notch. Although CT tests are considered in this section as application tests, they were used to calibrate the mesh regularisation input for each material, as addressed in Section 4.

Wide compact tensions (WCT) tests were performed with a similar setup, but with (i) rectangular specimens (120x60mm²), (ii) notch lengths of 30 or 40 mm, and (iii) the notch tip was sharpened

Table 1: Average and co-variation (in percentage) of web sections of all materials' mechanical properties.
[1] Results obtained with *Iosipescu* tests.
[2] Results obtained with 10° Off-Axis Tensile tests.

Property	I200-FC		I150-AP		I150-ST		I152-CP		U150-ST		S120-AP	
	Av.	CoV	Av.	CoV	Av.	CoV	Av.	CoV	Av.	CoV	Av.	CoV
E_{11}^+ [GPa]	29.6	5.3	-	-	29.4	8.2	25.2	5.9	26.6	5.2	32.7	9.3
S_{11}^+ [MPa]	322.6	3.2	-	-	376.4	4.8	426.0	3.4	347.1	2.9	326.2	5.2
E_{22}^+ [GPa]	17.6	18.1	-	-	8.4	12.6	10.9	7.3	8.7	15.0	-	-
S_{22}^+ [MPa]	70.7	2.6	-	-	33.8	17.9	121.3	7.0	69.5	8.8	-	-
E_{11}^- [GPa]	29.9	6.3	-	-	28.1	11.9	24.6	3.0	25.8	10.1	21.2	15.3
S_{11}^- [MPa]	441.5	6.5	-	-	550.5	12.8	436.9	6.0	450.6	5.1	435.1	12.1
E_{22}^- [GPa]	10.9	11.2	-	-	12.9	14.7	11.3	7.3	7.0	7.1	4.8	17.6
S_{22}^- [MPa]	121.6	13.7	-	-	122.7	6.9	104.2	10.6	83.5	8.5	88.9	18.3
G_{12} [GPa] [1]	2.89	12.1	3.01	6.7	3.17	11.0	4.24	15.0	4.16	14.2	-	-
S_{12} [MPa] [1]	67.1	2.9	46.8	8.5	69.8	7.0	65.3	3.3	70.8	8.7	41.4	15.0
G_{12} [GPa] [2]	-	-	4.70	2.7	-	-	-	-	-	-	3.45	12.6
S_{12} [MPa] [2]	-	-	20.4	9.7	-	-	-	-	-	-	16.8	19.9

with a 0.3 mm diameter wire saw.

Compact compression (CC) tests were performed with 120x120mm^2 square specimens which presented a triangular shaped notch with 40 or 45 mm of length, ending with a semi-circular corner with a 2 mm radius. The displacements were measured with crack mouth closing displacement points (CMCD), which are also near the notch and in the same vertical axis as the centre of the holes.

The CT, WCT and CC tests were performed for materials I200-FC, I150-ST, I152-CP and U150-ST.

For web-crippling (WC) tests, two different configurations were used - internal two flanges (ITF) and external two flanges (ETF). For I200-FC and I150-ST materials, the ETF configuration was tested with a bearing length of 15 mm, while for I152-CP, the same configuration test was performed with a bearing length of 100 mm. For all three materials, the ITF configuration tests were performed with 100 mm of bearing length. As for the displacements, two different sets were registered: (i) cross-head displacement of the test machine, which was used to plot load *vs.* displacement curves, and (ii) displacement of the web's upper and lowest points (excluding the web-flange junction region), which were used to compute the tests' stiffness.

For the double-lap (DL) tests (only I150-AP and S120-AP), specimens were cut with dimensions of 350x40mm^2 and a hole with 8 mm of diameter was drilled at different edge distances: (i) 15 mm (DL-15); (ii) 25 mm (DL-25); (iii) 35 mm (DL-35); (iv) 70 mm (DL-70); and (v) two bolts with edge distance and inner spacing of 35 mm (DL-2B). The displacements were imposed on the farthest free edge from the hole, and a pined steel bolt was placed in the hole of the specimens.

4. Calibration of the model for new materials

4.1. Description of FE models

Since one of the main objectives of the damage model developed is to minimise the computational costs, simplifications and symmetry boundary conditions were used in the FE models whenever possible. For all models, C3D8R elements (8-node brick element with reduced integration) were used for the mesh, always with "enhanced hourglass control". "Mesh controls" were always assigned with the main priority of generating a regular cuboid-element mesh to avoid the possible influence of the mesh regularisation factor in the results. Implicit analysis were conducted for all models allowing for a maximum residual flux norm of 1%, except for severe discontinuity iterations, for which that value was increased to 5%.

Tensile tests were modelled with triple symmetry boundary conditions. To force the failure to occur in the centre of the specimen, a "weak region" with 1 mm^2 of area and through the entire thickness was introduced. This region was modelled with the same material as the rest of the specimen, except for the limit strains ($\epsilon_{ii,u}^{\pm}$ and $\gamma_{ij,u}$), which were reduced to 90% of the original values.

For the 10° OAT tests, only one symmetry boundary condition in the thickness direction was used. There was no "weaker region" since the numerical failure starts near the edges of the specimen and not at the centre (*cf.* Section 4.4).

Compressive tests, although obtained with 2 different standards (*cf.* Section 3.1), were always modelled with the same "weaker region" as their tensile counterparts, but with double symmetry boundary conditions only (Figure 1 (a)). The length was fully modelled due to the effect of the fixed-end boundary
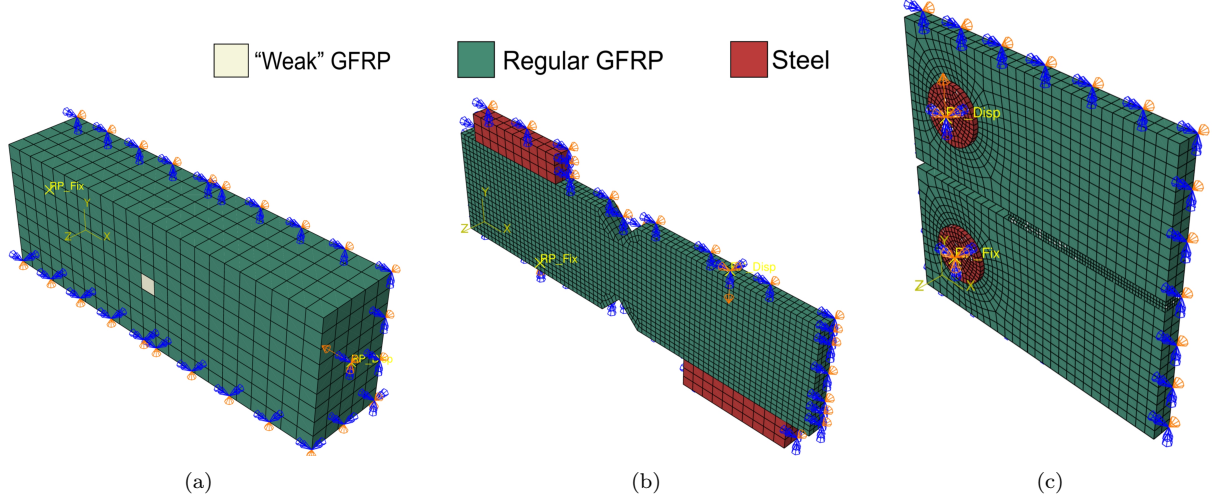
Figure 1: Mesh and boundary conditions of FE models: (a) 1 mm mesh for longitudinal compressive tests; (b) 1 mm mesh for *Iosipescu* tests; (c) 0.6 mm detailed mesh for compact tension tests.

conditions on the stress distribution, which consequently resulted in an undesirable failure mode.

For the *Iosipescu* tests' modelling, symmetry boundary conditions were applied only at mid-thickness. The displacement and fixed boundary conditions were applied directly in the top right and bottom left faces of the specimen, respectively (Figure 1 (b)). Additionally, two steel parts were added ($E_s = 200$ GPa and $\nu_s = 0.3$) on the top left and bottom right faces, as in the experimental setup standard. The contact between the steel parts and the GFRP material was defined with a "finite sliding" formulation, a "hard contact" normal behaviour, and a "penalty" formulation with a 0.1 friction coefficient.

As for the compact tension tests, only one symmetry boundary condition at mid-thickness was used, and the same contact formulation as in the *Iosipescu* tests was applied between the steel pins and their respective coaxial surface of the specimen. Moreover, to lower the computational costs of the mesh sensitivity analysis, the area near the notch where the stress distributions were expected to be more intricate was meshed independently of the remainder of the specimen, as seen in Figure 1 (c).

4.2. Calibration process and assumptions

The model only considers one elastic modulus for each direction as input (E_{ii} instead of E_{ii}^+ and E_{ii}^-). For this study, the author decided to use the elastic moduli retrieved from the tensile tests, since, for some of the experimental compressive tests, not all guidelines were thoroughly followed. Additionally, regarding the transverse elastic modulus (E_{22}), and given the non-linear behaviour of the experimental stress *vs.* strain curves, the values used as input (and presented earlier in Table 1) were retrieved

from the first linear stage, approximately between 5 and 10 MPa.

Other simplifications regarding properties where no experimental data was available were done. For the through-thickness elasticity modulus (E_{33}) and ultimate strengths (S_{33}^+ and S_{33}^-) inputs, the same values to those found in the literature for similar GFRP materials were used [5]. Moreover, for the shear moduli G_{13} and G_{23}, the G_{12} values retrieved in Section 3.1 were adopted, and for the Poisson coefficients (with the exception of I200-FC) and ultimate shear strengths for planes 12 and 13, the I150-AP material values were adopted. This material is already calibrated in [5].

Regarding the residual strength control inputs, the ultimate strains ($\epsilon_{ii,u}^{\pm}$ and $\gamma_{ij,u}$) were computed as the ratio between ultimate stress and the elastic modulus (for linear cases), or directly from the stress *vs.* strain curves, for non-linear cases. The residual strength inputs ($r_{ii}^{\pm}$ and r_{ij}) are the ratio between the residual stress and the ultimate stress.

The damage progression control inputs ($d_{i,max}^{\pm}$ and $m_i^{\pm}$) were calibrated through a curve fitting process, for every experimental test available.

As for the mesh regularisation parameter (α) and the 9 viscous regularisation parameters ($\eta_i^{\pm}$), the initial calibration process (for coupon tests) was performed with an $\alpha = 15$mm and an $\eta_i^{\pm}=1\times10^{-5}$. Nonetheless, the mesh regularisation parameter was duly calibrated with the CT test, as shown in Section 4.4, and in more complex cases such as the application tests (*cf.* Section 5), the viscous regularisation parameter was increased to $\eta_i^{\pm}=1\times10^{-3}$ due to convergence difficulties.

For every calibration input where no experimental data was available, the I150-AP inputs calibrated in [5] were used.

4.3. Mesh study

This preliminary study regarding the mesh sensitivity analysis, which aims to find a mesh that achieves a better compromise between the computational costs and the proximity with the experimental data, was performed for the I200-FC-W material for each test (except for the OAT test, for which the material I150-AP-W was used).

For LT, TT, LC and TC tests, the study was performed for meshes of 1 mm, 0.5 mm, and 0.25 mm. Regarding elastic moduli ($E_{ii}^{\pm}$), the relative difference when compared with experimental data was negligible for all meshes and tests. As for the maximum load, the highest variation in relative difference (between 1 mm and 0.25 mm meshes) registered was of 1.1 percentage points (p.p.). These results show that a coarser mesh of 1 mm (Figure 1 (a)) already presents stabilized results.

For the *Iosipescu* test study, meshes of 2 mm, 1 mm, and 0.5 mm were used. Relative differences regarding the shear modulus were also insignificant. As for the maximum loads, a 2 mm mesh presented 7.0% overestimation and a 1 mm mesh resulted in -0.8%. The 0.5 mm mesh presented convergence problems. These results led to the adoption of a 1 mm mesh for all *Iosipescu* tests (Figure 1 (b)).

Regarding the 10° OAT tests, meshes of 3 mm, 1.5 mm and 0.75 mm were used, with negligible difference in stiffness between them. For the maximum loads, varying the mesh from 3 mm to 1.5 mm produces a change of 4.6 p.p., and from 1.5 mm to 0.75 mm results in a change of 2.5 p.p., showing that for a mesh of 1.5 mm the results are already good. The mesh view of this model is similar to the one presented in Figure 1 (a), but without the "weak" region

Finally, for the CT test, the mesh study was only performed in the notch area, with meshes of 0.6 mm, 0.3 mm and 0.15 mm used. The remain-der of the specimen is constituted by approximately cubic elements with 2.5 mm, which corresponds to half the thickness used in FE models in the case of I200-FC. The difference in stiffness between all meshes was once more negligible, and the variation of the maximum load relative differences is of 2.7 p.p. (between 0.6 and 0.3 mm) and 1.1 p.p. (between 0.3 and 0.15 mm). Although the results are more stabilized for a 0.3 mm mesh, the 0.6 mm mesh allows for better convergence, therefore it is used for other materials (Figure 1 (c)).

4.4. Results and discussion

The numerical results obtained are compared in two forms: (i) in stress *vs.* strain curves, the behaviour until failure is analysed and the main values are compared; and (ii) in load *vs.* displacement curves, the failure and post-failure behaviour is compared. The final damage progression calibration parameters are presented in Table 2 for all materials tested, and Figure 2 shows numerical and experimental curves for some of the tests performed.

For longitudinal tests (both tensile and compressive), due to their linearity, the calibration results present very good agreement with experimental data. Elastic modulus and ultimate stress predictions were always within 5% and 8% of the experimental average, respectively, except for the LC test of the S120-AP, which presented overestimations of $\approx$50%. This occurred due to the different standard used to retrieve the mechanical properties in compression for this material (*cf.* Section 3.1).

For transverse tensile tests, all materials tested presented a distinct bi-linear behaviour. Elastic moduli predictions were within a 3% and 13% relative difference when compared to experimental averages, and the ultimate stress maximum relative difference registered was 1.6%, confirming very good agreement between experimental and numer-
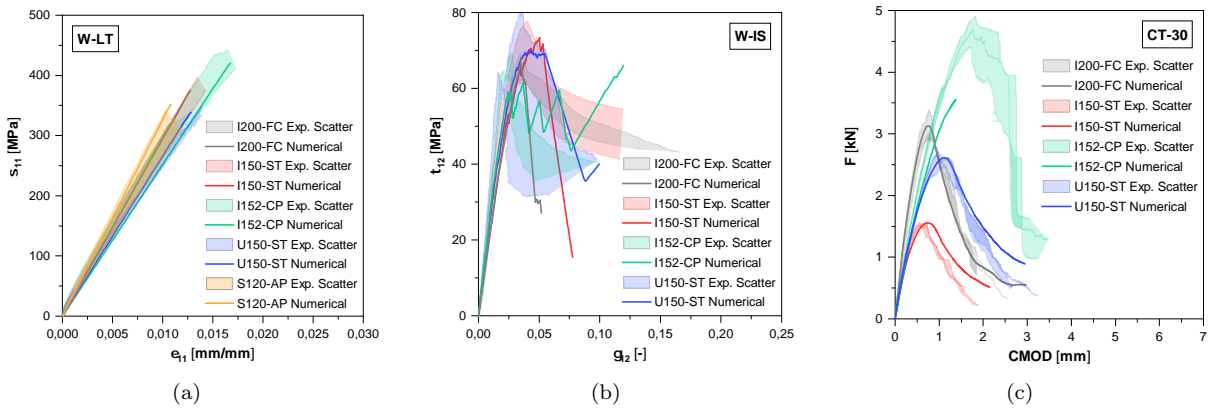

Figure 2: Calibration results: (a) experimental and numerical stress *vs.* strain curves for longitudinal tensile tests; (b) experimental and numerical stress *vs.* strain curves for *Iosipescu* tests; (c) experimental and numerical load *vs.* CMOD curves for compact tensions tests

Table 2: Damage control inputs and mesh regularisation parameter of web sections for all materials.
[1] Results obtained with *Iosipescu* tests.
[2] Results obtained with 10° Off-Axis Tensile tests.

| Material	$d_{1,max}^+$	$d_{2,max}^+$	$d_{1,max}^-$	$d_{2,max}^-$	$d_{4,max}$	m_1^+	m_2^+	m_1^-	m_2^-	m_4	α [m]
I200-FC	0.001	0.8	0.001	0.4	0.95^1	10	0.8	10	0.7	5^1	0.03
I150-AP	-	-	-	-	0.95^2	-	-	-	-	0.4^2	-
I150-ST	0.001	0.8	0.001	0.4	0.99^1	10	0.8	10	2	5^1	0.04
I152-CP	0.001	0.6	0.001	0.2	0.90^1	10	1	10	5	5^1	0.05
U150-ST	0.001	0.6	0.001	0.4	0.95^1	10	0.8	10	0.5	5^1	0.03
S120-AP	0.001	-	0.001	0.5	0.97^2	10	-	10	10	0.3^2	-

ical data.

Regarding transverse compressive tests, some materials presented linear behaviour, while others showed slight exponential stress *vs.* strain curves. For this reason, and due to the use of the transverse tensile elastic modulus (E_{22}^+), some compromises had to be reached regarding the damage control inputs. Nonetheless, numerical curves were within the experimental scatter and ultimate stress relative differences were always lower than 6%, except for I200-FC, which presented an overestimation of 13.6%. As for the elastic modulus, values below a 6% relative difference were also obtained, with exception of I200-FC and I150-ST, which presented differences of 40.7% and -34.6%, respectively.

Iosipescu tests were successfully calibrated (Figure 2 (b)), although a consistent underestimation between 20% and 35% regarding the shear modulus prediction was made. This is probably related to the experimental methodology used to compute the shear modulus, which was replicated in the numerical simulation. As for ultimate shear stress values, a maximum relative difference of 8.7% was registered.

The 10° OAT tests also presented good agreement with experimental data, with maximum relative differences with relation to experimental data of 2.4% and 1.1% regarding the shear modulus and ultimate shear stress, respectively. Nevertheless, there was an earlier damage onset than expected concerning the shear modulus, due to the very low exponential evolution input (m_4), as seen in Table 2.

Finally, the compact tension tests also presented good agreement with experimental data for most materials (Figure 2 (c)). The only exception was the I152-CP for 30 mm notch length tests, where convergence was not achieved. Stiffness and maximum load numerical results were mostly around 5% of relative difference when compared to experimental averages, except some cases where a relative difference of ≈12% was registered. The post-failure behaviour was also well depicted, both in load *vs.* displacement curves and in numerical simulations, with a crack propagating along the notch (evident by a total degradation of the transverse elastic modulus), as was registered in experimental specimens (Figure 3). Additionally, for the I152-CP, where experimental specimens presented delamination due to compressive failure on the opposite side of the notch, numerical models were also able to capture this behaviour, with clear out-of-plane displacements in the same region as the experimental specimens.
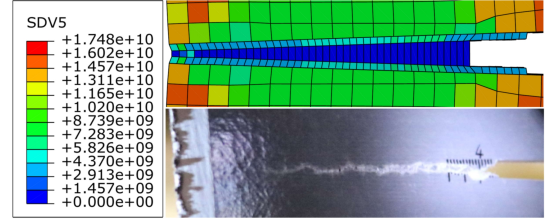
Figure 3: Experimental and numerical failure (degradation of E_{22} (SDV5) in Pa) of a CT specimen.

5. Application of the model

5.1. Description of FE models

For all FE models used for application tests, the same considerations presented initially in Section 4.1 were followed.

Wide compact tension (WCT) tests were modelled with mid-thickness symmetry boundary conditions, and the region near the notch was meshed meshed independently, similarly to the CT tests shown in Figure 1 (c). The coarser mesh region was meshed with 2 elements across the thickness direction. The interaction between the steel pins and the specimen was defined with the same contact formulation mentioned in Section 4.1 for *Iosipescu* tests.

Compact compression (CC) tests were modelled with all the same simplifications as mentioned for the WCT above. Additionally, an initial study comparing a semi-circular notch tip with a sharp notch tip was made, concluding that the former induced earlier damage propagation resulting in lower ultimate loads. Hence, a sharp notch tip was chosen. Figure 4 (a) shows a numerical model of a CC test.
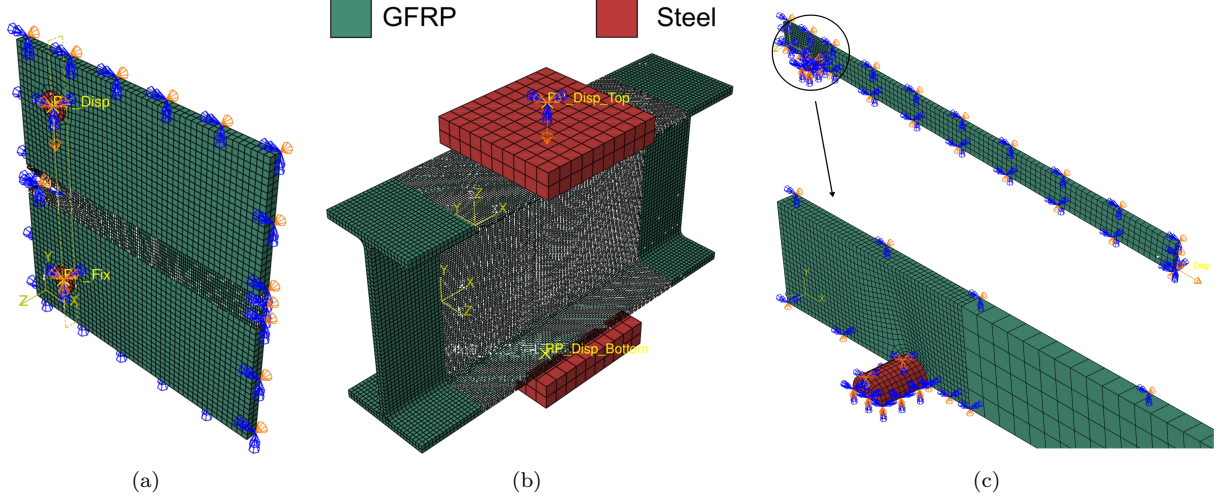
Web-crippling (WC) tests, depending on the ex-

Figure 4: Mesh and boundary conditions of FE models: (a) 1 mm detailed mesh for CC tests; (b) 1.5 mm detailed mesh for WC-ITF tests (complete model); (c) 0.5 mm detailed mesh for DL tests.

perimental failure mode characteristics, were modelled in two different ways: (i) simplified models, for crushing failure profiles (I200-FC and I150-ST); and (ii) complete models, for buckling and mixed failure profiles (I152-CP). Simplified models were modelled with triple symmetry boundary conditions for ITF configurations and double symmetry for ETF configurations. For the complete models, non-linear geometric analyses were conducted, with an initial imperfection of 0.01 mm of amplitude corresponding to the critical buckling mode. For all models, the contact formulation between the cross-head and the profile was the same as in other application tests. The web-flange junctions were modelled with the web material properties. To reduce computational costs, the mesh refinement was performed only in the regions where stress distributions were non-uniform, with the coarser mesh zones being meshed with half-thickness sized elements. Figure 4 (b) depicts a complete model with an ITF configuration.

As for double-lap (DL) tests, double symmetry (width and thickness) boundary conditions were used. The same contact formulation as other tests was used between the steel bolt and the GFRP specimen. The region between the end face (opposite to the loaded end) and the centre of the bolt plus 15 mm was considered for the mesh refinement study, with the remaining specimen meshed with 4 mm sized elements. A model of a DL test is represented in Figure 4 (c).

5.2. Mesh study

The mesh study was performed for the I200-FC material, except for the double-lap tests, where the I150-AP was used. All results were obtained with the calibration obtained in Section 4, with the only

difference being the viscous regularisation parameter, where the highest possible value that did not affect the results was used $\eta_i^{\pm} = 1 \times 10^{-3}$.

For WCT tests (30 mm notch length), meshes of 1 mm, 0.5 mm, and 0.25 mm in the notch region (similar to Figure 1 (c)) were considered for this study. The results presented relative differences with respect to experimental averages of 18.5% (1 mm), 17.3% (0.5 mm), and 16.7% (0.25 mm) regarding stiffness values, and 2.6%, -6.5%, and -7.1% regarding maximum load values. A mesh of 0.5 mm was considered for all other materials, given the stabilization of the maximum load is evident for this mesh size.

For CC tests (40 mm notch length), the mesh study was performed for mesh sizes of 2 mm, 1 mm and 0.5 mm in the notch region. This resulted in relative differences of 21.2% (2 mm), 20.3% (1 mm), and 19.8% (0.5 mm) for stiffness values, and 27.5%, 24.5%, and 24.0% for maximum load values. The results for a 1 mm detailed mesh size (Figure 4 (a)) presented a better compromise between computational cost and stabilized stiffness and maximum load predictions, therefore, they were used for all materials.

Regarding web-crippling tests, the mesh study presented concerns the ITF-100 configuration (100 mm of bearing length) only. The mesh refinement was done with 5 mm (half-thickness), 2.5 mm, and 1.25 mm. Stiffness variations were negligible, and maximum load predictions presented relative differences in relation to experimental results of 35.4%, 21.5% and 21.7%, for 5 mm, 2.5mm and 1.25 mm meshes, respectively. These results show that a mesh of 2.5 mm (quarter-thickness) presents a better compromise

(Figure 4 (b)). For other materials, detailed meshes of a quarter thickness were also used (2 mm for I150-ST and 1.5 mm for I152-CP).

For double-lap tests, the study was performed for the DL-15 configuration. 2 mm, 1 mm and 0.5 mm meshes were used in the detailed mesh region. Given the doubts regarding the experimental stiffness measurements, these values were not used for this study. As for maximum load predictions, the results presented relative differences of 58.9% (2 mm), 17.3% (1 mm), and 14.3% (0.5 mm). Although the results for a 1 mm mesh are good enough regarding the maximum load prediction, the post-failure behaviour was not well depicted. For this reason, a 0.5 mm detailed mesh was used for all materials and test configurations (Figure 4 (c)).

5.3. Results and discussion

5.3.1. Wide compact tension tests

For the WCT models, the load *vs.* CMOD curves showed good agreement with experimental data and present a similar behaviour to the CT tests presented earlier in Figure 2 (c). Stiffness values presented relative differences up to ≈25% when compared to experimental data. However, this difference may be emphasised by the small interval used to compute the stiffness (*cf.* Section 3.2). For all materials, except for I152-CP, maximum load predictions presented always lower relative differences than 13.5%. For I152-CP, there were convergence difficulties, and an additional non-linear analysis was performed, which overestimated the maximum load by 23.7%, but allowed for the development of the softening stage.

As for the failure modes, WCT simulations for I200-FC, I150-ST and U150-ST were in accordance with experimental data, with a crack propagating from the notch tip and along the longitudinal direction (similarly to Figure 3). For I152-CP, simulations that did not converge presented damage in the load application holes (similarly to experimental data for this material), but the experimental out-of-plane displacements registered experimentally for 40 mm notch length specimens were not captured in numerical results, even when considering a non-linear analysis.

5.3.2. Compact compression tests

The compact compression tests load *vs.* CMCD curves presented good agreement with experimental data in the first loading stage, but near the maximum load and the final softening stage, the behaviour was more difficult to capture, as seen in Figure 6 (a). I150-ST and I152-CP materials presented very good stiffness predictions with relative differences to experimental data below 2%. I200-FC and U150-ST results' were overestimated in 20.3% and 8.4%, respectively, due to the highest differ-

ence between their tensile and compressive transverse elastic modulus (*cf.* Table 1). Maximum load predictions were all under 12% of relative difference to the experimental averages, except for I200-FC, where, mainly due to the aforementioned difference in elastic moduli, a relative difference of 24.5% was registered.

Additionally, the load *vs.* CMCD curves near the maximum load region were compromised by displacement fluctuations that were not expected. These fluctuations are associated with transverse elastic modulus degradation in the GFRP specimen near the load application holes caused by the high stress concentrations in these zones. In fact, all numerical models presented this type of failure simultaneously to the propagation of a kink band that started in the notch tip and propagated in the longitudinal direction, as registered in all experimental tests. Particularly for I152-CP and U150-ST materials, out-of-plane displacements were also registered, but even when considering non-linear analyses, this failure mode was not depicted numerically.

An additional parametric study on the residual strength for I200-FC was performed, given this material presented a particularly high input ($r_2^- = 0.5$) which was probably overestimated due to the CLC standard used to retrieve these properties. The results (also depicted in Figure 6 (a)) showed that, for an $r_2^- = 0.4$, the model was able to converge, and tensile failure in the opposite side of the notch was depicted in numerical simulations, similarly to experimental tests for I200-FC and I150-ST (Figure 5), leading to believe that the true residual strength of this material should be closer to 0.4. For other materials, however, no significant improvements were obtained.
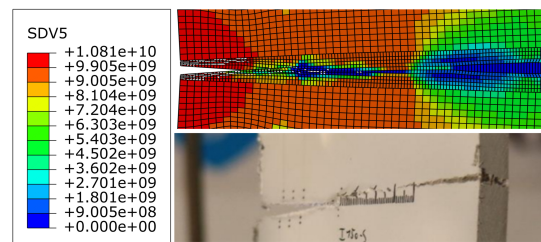

Figure 5: Experimental and numerical failure (degradation of E_{22} (SDV5) in Pa) of a CC specimen.

5.3.3. Web-crippling tests

For the web-crippling results, the load *vs.* displacement curves shown in Figure 6 (b) were obtained with cross head displacements and were adjusted to fit experimental data. Therefore, stiffness results are not directly related to the curves presented.

The results also show good agreement with experimental data. For I200-FC (both configurations tested), stiffness and maximum load predictions
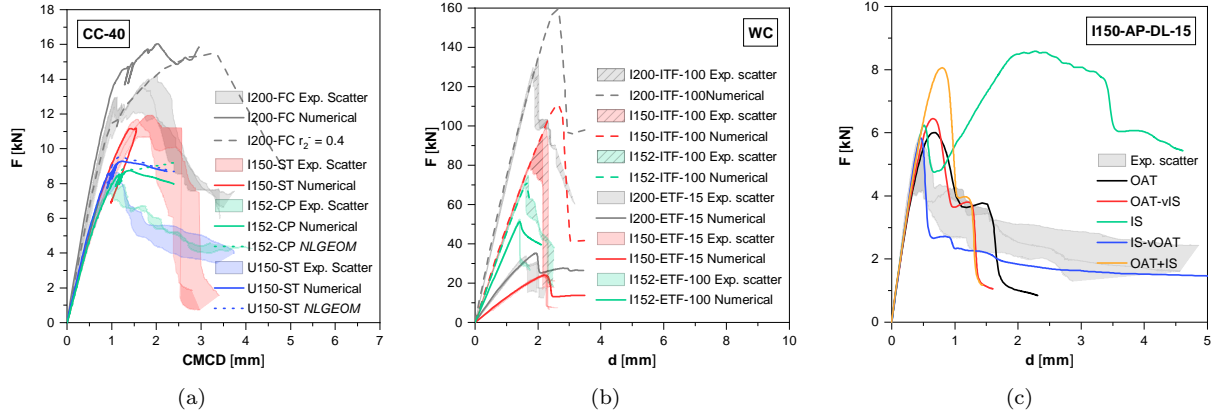
8

Figure 6: Application results - experimental and numerical load *vs.* displacement curves for: (a) compact compression tests with a 40 mm notch length; (b) web-crippling tests for all configurations tested (I section profiles only); (c) I150-AP double-lap tests with a 15 mm bolt-edge distance.

presented relative differences regarding experimental results between 10% and 20%, mainly due to the aforementioned difference in compressive and tensile transverse elastic moduli. I150-ST results present relative differences below 10%, except for the maximum load in the ITF-100 configuration. This particular overestimation in 20.7% may be related to the simplification of the web-flange properties, which are known to be potentially weaker. As for the I152-CP material, both configurations registered very low relative differences regarding stiffness and maximum load values (below 1%), except for ITF-100, where the stiffness was underestimated in 9.4% (still very good). Additionally, for all cases, the residual load stage was considerably higher in numerical simulations than in experimental results, which can be associated with the aforementioned overestimation of the residual strength input r_2^-.

The failure modes for these materials were also well depicted. Both configurations of I200-FC and I150-ST tests presented crushing failure in the web-flange junction near the bearing plates, as was registered experimentally. For I152-CP, also in both configurations, the use of non-linear analyses allowed for out-of-plane displacements (buckling failure) in the same manner as experimental tests (Figure 7).
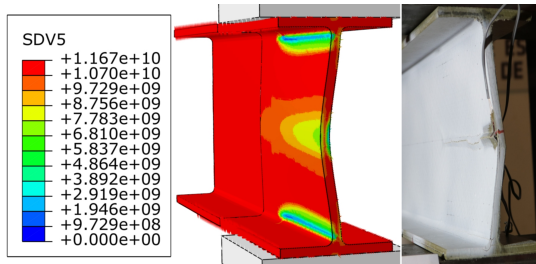

Figure 7: Experimental and numerical failure of a WC-ETF-100 specimen.

5.3.4. Double-lap tests

The double-lap tests were performed not only to assess the agreement between experimental and numerical results, but also to understand which calibration of in-plane shear properties (G_{12}, S_{12}, $d_{4,max}$, m_4, γ_{12}, and r_{12}) better characterises the material (*Iosipescu* or 10° OAT tests). Table 3 presents the summary of the main calibration sets used, for I150-AP only, and Figure 6 (c) shows the adjusted load *vs.* displacement curves for the DL-15 configuration.

Table 3: Different sets of in-plane shear calibration variables tested in double-lap tests.

Property	I150-AP			
	OAT	OAT-vIS	IS	IS-vOAT
G_{12} [GPa]	4.70	3.01	3.01	4.70
S_{12} [MPa]	20.36	46.76	46.76	46.76
$d_{4,max}$	0.95	0.95	0.95	0.95
m_4	0.4	0.4	5	5
$\gamma_{12,u}$	0.024	0.024	1	0.024
r_{12}	0.01	0.01	1	0.01

The results show that "IS" properties can be discarded due to the high residual load stage, which does no exist in experimental results (all specimens presented shear-out failure for this configuration, which resulted in a low residual load stage). The sets "OAT" and "OAT-vIS", although presenting reasonable maximum load predictions (relative differences between 14% and 23% compared to experimental results) and good post-failure behaviour, registered a decrease in stiffness near the maximum load, that occurs because of the small m_4 used. This decrease in stiffness is not registered in experimental curves. Finally, the "IS-vOAT" properties

9

presented the best results, with the maximum load overestimated only in 11.4% (the lowest obtained) and good curve agreement in all stages. Figure 8 compares a numerical simulation with this set of properties to the experimental failure registered.
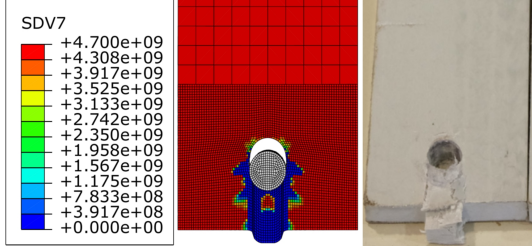

Figure 8: Experimental and numerical failure (degradation of G_{12} (SDV7) in Pa) of a DL-15 specimen.

For DL-25 and DL-35, where shear-out was also the only experimental failure mechanism, the results followed the same trend as the DL-15 presented above. For DL-70, the high residual load registered experimentally was not captured numerically due to the inability of the implicit analysis to "transfer" the stiffness of the material to the adjacent elements of the failed ones. Nevertheless, numerical load *vs.* displacement curves with different set of properties showed similar characteristics to the DL-15 tests, although with less variability between themselves. As for DL-2B, shear-out and bearing failure were registered somewhat simultaneously in experimental tests, and numerical simulations successfully captured both.

6. Conclusions and future developments
The main goal of this study was the assessment of the validity of a new progressive failure model for pultruded FRP. With this in mind, the calibration of the model for 6 new materials was performed, and the validation of the model was attested by simulating several application tests.

The calibration process was deemed successful for every test performed. Longitudinal (tensile and compressive) tests and transverse tensile tests presented excellent agreement with experimental data regarding curve behaviour, elastic modulus and ultimate stress predictions. Transverse compressive tests, *Iosipescu* tests and 10° OAT tests , although presenting some difficulties in the calibration process, were also successfully calibrated. The compact tension tests used to calibrate the mesh regularisation parameter also showed very good results, except for one material which presented convergence difficulties.

The application tests used to validate the model were also in good agreement with experimental data. The results regarding wide compact tension tests showed that the calibration of the mesh

regularisation parameter was successful. Compact compression tests, however, presented more intricate results, with an early damage onset near the load application holes that hindered the development of the softening stage in the numerical models. Nonetheless, for materials with similar E_{22}^+ and E_{22}^-, maximum load relative differences were under 12%. Web-crippling tests for profiles with an I section presented also very good agreement with experimental data. For the double-lap tests, the results showed that the set of properties "IS-vOAT", which considers damage progression control inputs and the ultimate shear stress of the *Iosipescu* test, and residual strength inputs and the shear modulus of the OAT test, presents better agreement with experimental data.

Overall, the results presented in this work show that it is possible to predict the failure loads, modes, and post-failure behaviour under several different actions, for a significant range of pultruded GFRP materials.

Nevertheless, to improve the results obtained, some alterations to the model are suggested: (i) adopt different tensile and compressive elastic modulus, and (ii) modify the current UMAT to a VUMAT (which is used for explicit analysis). The former would facilitate the calibration process and increase the prediction capabilities of application tests where both tensile and compressive stresses are present. The latter would allow for element removal and would better predict, for example, the bearing failure effect in the DL-70 test.

References
[1] P. P. Camanho. Failure criteria for fibre-reinforced polymer composites. *Faculdade de Engenharia da Universidade do Porto*, 2002.

[2] S. Tsai. Strength Characteristics of Composite Materials. *NASA CR-224*, 1965.

[3] S. Tsai and E. Wu. A General Theory of Strength for Anisotropic Materials. *Journal of Composite Materials*, 5(1):58–80, Jan 1971.

[4] Z. Hashin. Failure Criteria for Unidirectional Fiber Composites. *Journal of Applied Mechanics*, 47(2): 329–334, Jun 1980.

[5] J. A. Gonilha, N. Silvestre, J. R. Correia, V. Tita, and D. Martins. Novel progressive failure model for quasi-orthotropic pultruded FRP structures: Formulation and calibration of parameters (Part I). *Composite Structures*, 255:112974, Jan 2021.

[6] J. M. Hodgkinson. *Mechanical Testing of Advanced Fibre Composites*. Woodhead Publishing, Boca Raton, FL, 2000.